

Point target detection and subpixel position estimation in optical imagery

Vincent Samson, Frédéric Champagnat, and Jean-François Giovannelli

We address the issue of distinguishing point objects from a cluttered background and estimating their position by image processing. We are interested in the specific context in which the object's signature varies significantly relative to its random subpixel location because of aliasing. The conventional matched filter neglects this phenomenon and causes a consistent degradation of detection performance. Thus alternative detectors are proposed, and numerical results show the improvement brought by approximate and generalized likelihood-ratio tests compared with pixel-matched filtering. We also study the performance of two types of subpixel position estimator. Finally, we put forward the major influence of sensor design on both estimation and point object detection. © 2004 Optical Society of America

OCIS codes: 040.1880, 100.5010, 100.0100.

1. Introduction

We tackle the problem of subpixel object detection in image sequences that arises, for instance, in infrared search-and-track applications. In this context the target signature is proportional to

$$\mathbf{s}_\epsilon[i, j] = \int_{i-0.5}^{i+0.5} \int_{j-0.5}^{j+0.5} h_o(u - \epsilon_1, v - \epsilon_2) du dv, \quad (1)$$

where $\mathbf{s}_\epsilon[i, j]$ represents the percentage of light intensity at pixel (i, j) , $\epsilon = (\epsilon_1, \epsilon_2)$ refers to the object's random subpixel position, and h_o is the optical point-spread function (PSF). According to common sensor design, the energy of the signal component, $\mathbf{s} = \alpha \mathbf{s}_\epsilon$, is almost entirely concentrated on a single pixel. However, unlike for amplitude α , which is unknown too, its dependence on location parameter ϵ is highly nonlinear. Its influence in our application is rather significant because of aliasing and, unless a velocity model is available, an object's subpixel position is hardly predictable from frame to frame. Common

sensor design leads to an image spot that is down-sampled by almost a factor of 5. We can see from Fig. 1 the energy loss at the central pixel relative to subpixel location and the random change in spatial pattern that is due to aliasing. This phenomenon has a major effect on detection performance, as we show below. To our knowledge, this pitfall has not been addressed yet in the literature. The prevailing opinion is that there is no signature information on subpixel objects. Indeed, the various authors who dealt with small-object detection concentrated on clutter removal,¹⁻³ multispectral or hyperspectral fusion,^{4,5} and multiframe tracking methods.⁶⁻⁸ We focus here on the processing of a single frame. In Section 2 we formulate the detection problem in the classic model of a signal in additive Gaussian noise.⁹ When the signal is deterministic, Neyman-Pearson strategy yields the conventional matched filter. In the present case, the signal from the target depends on unknown parameters, and we have to deal with a composite hypothesis test. A common procedure is given by the generalized likelihood-ratio test. But so-called nuisance parameters α and ϵ can also be considered random variables with known distributions (some *a priori* density functions in the Bayesian terminology); then the straightforward extension of the likelihood-ratio test is to integrate the conditional distribution over α and ϵ . When we were modeling the signal component as a sample function we could also think of the class of random signal in noise-detection problems, which have been studied primarily in the Gaussian case. Unfortunately, when \mathbf{s}_ϵ is

V. Samson (vsamson@irisa.fr) and F. Champagnat are with the Office National d'Études et de Recherches Aéronautiques, 29, Avenue de la Division Leclerc, 92322 Châtillon Cedex, France. J.-F. Giovannelli is with the Laboratoire des Signaux et Systèmes, Supélec, Plateau de Moulon, 91192 Gif-sur-Yvette Cedex, France.

Received 16 May 2003; revised manuscript received 6 August 2003; accepted 11 August 2003.

0003-6935/04/020257-07\$15.00/0

© 2004 Optical Society of America

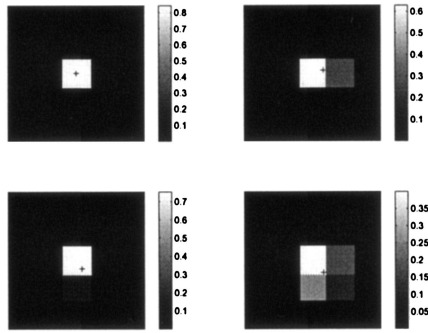


Fig. 1. Examples of image spots for several cross-marked subpixel positions (windows of size 5×5 pixels). Sensor design parameter r_c is set to its common value of 2.44 (see Section 3).

considered a random vector, its empirical distribution proves to be highly non-Gaussian when ϵ is uniformly sampled.

For instance, the histogram of the central pixel depicted in Fig. 2 shows that a Gaussian fit is not satisfactory at all. In Section 3 we define more precisely the optical system model used in our numerical experiments. We consider both Gaussian white noise and fractal noise of unknown correlations generated by a standard technique of spectral synthesis. Section 4 is devoted to the position-estimation problem, i.e., estimation of parameter ϵ . We propose two estimators that take into account the fact that signal amplitude α is also unknown. We demonstrate the performance of these estimators in terms of mean-square errors (MSEs). As for the detection problem, we finally illustrate the expected improvement in quality brought by correctly sampled optics compared with common sensor design.

2. Detection Problem

We consider a local detection window sliding across the image. The problem is to decide whether an object is present at the window's central pixel. Its solution involves a binary test that typically reads as follows:

$$\begin{aligned} H_0 &: \mathbf{z} = \mathbf{n}, \\ H_1 &: \mathbf{z} = \alpha \mathbf{s}_\epsilon + \mathbf{n}, \end{aligned} \quad (2)$$

where \mathbf{z} is the vector that collects the window data, $\mathbf{s} = \alpha \mathbf{s}_\epsilon$ is the object response (signal vector), and \mathbf{n} is

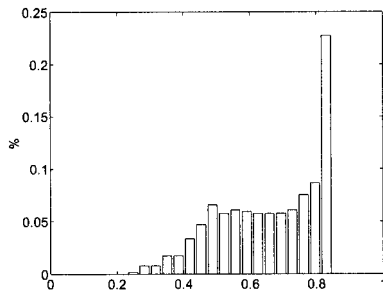


Fig. 2. Empirical distribution of the image-spot central pixel $s_\epsilon[0, 0]$ for a uniformly random position $\epsilon \sim \mathcal{U}_{[-0.5, 0.5]^2}$.

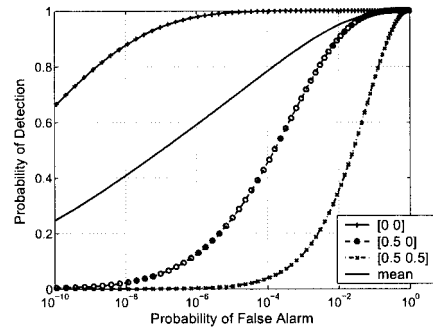


Fig. 3. Examples of PMF theoretical ROC curves for several true subpixel positions (SNR, 15 dB): the ideal case, where $\epsilon^* = \epsilon_0 = (0, 0)$; $\epsilon^* = (0.5, 0)$; and the worst case, where $\epsilon^* = (0.5, 0.5)$. The mean curve was drawn for uniformly sampled ϵ^* .

the additive Gaussian noise. The signature shape is known and deterministic, so \mathbf{s} depends only on the two unknown parameters, $\alpha \in \mathbb{R}$ and $\epsilon \in \mathcal{E} = [-0.5, 0.5]^2$. Noise vector \mathbf{n} is assumed to be centered (in practice we first remove the empirical mean from the data) with a known or previously estimated covariance matrix \mathbf{R} . Thus, if we assume that \mathbf{n} is independent of \mathbf{s} , the following conditional distributions are Gaussian:

$$\begin{aligned} p(\mathbf{z}|H_0) &\sim \mathcal{N}(0, \mathbf{R}), \\ p(\mathbf{z}|H_1, \alpha, \epsilon) &\sim \mathcal{N}(\alpha \mathbf{s}_\epsilon, \mathbf{R}). \end{aligned} \quad (3)$$

Let us first assume that parameters α and ϵ are given. The problem amounts to a simple hypothesis test, which is to detect a deterministic signal in Gaussian noise. The Neyman–Pearson strategy, or likelihood-ratio test, is given by

$$\frac{p(\mathbf{z}|H_1, \alpha, \epsilon)}{p(\mathbf{z}|H_0)} \underset{H_0}{\overset{H_1}{\geq}} \text{threshold}. \quad (4)$$

It is equivalent to classical matched filtering, which simply compares the statistic $\alpha \mathcal{T}_\epsilon(\mathbf{z}) = \alpha \mathbf{s}_\epsilon^T \mathbf{R}^{-1} \mathbf{z}$ with some threshold.

A. Pixel-Matched Filtering

As the exact object location is unknown in practice, we could assume by default that $\epsilon = \epsilon_0 = (0, 0)$, i.e., that the object is at the center of the pixel, whereas the true location would correspond to $\epsilon = \epsilon^*$. Thus the detector, which consists in thresholding the pixel-matched filter (PMF) $\alpha \mathcal{T}_{\epsilon_0}(\mathbf{z})$, is optimum, provided that $\epsilon^* = \epsilon_0$. Otherwise it is mismatched and therefore suboptimum. Because the conditional distributions of $\mathcal{T}_{\epsilon_0}(\mathbf{z})$ under each assumption are Gaussian, we easily get the expression for the probability of detection P_d and of false alarm P_{fa} . The corresponding receiver operating characteristic (ROC) curves for critical values of ϵ^* are depicted in Fig. 3. They clearly show that the PMF performance worsens significantly as ϵ_0 differs from ϵ^* . But, beyond extreme situations (related to a true target location between two or four pixels instead of the center), the mean curve represents the average statistics over uniformly random positions. We can see that the price

paid for deviation from the ideal curve, if one neglects the random location, is rather high even at a favorable signal-to-noise (SNR) ratio. For a SNR of 15 dB and at a P_{fa} of 10^{-4} , the probability of detection decreases from nearly 1 to 0.8.

The object response also depends (linearly this time) on amplitude α , which is generally unknown. Yet, assuming strictly positive amplitude, we can see that, whenever $\alpha > 0$, thresholding $\alpha \mathcal{T}_{\epsilon_0}(\mathbf{z})$ gives the same ROC curve as thresholding $\mathcal{T}_{\epsilon_0}(\mathbf{z})$. Without any assumption about α , a classical solution is to estimate it by maximum-likelihood (ML) theory. Indeed under the assumption of Gaussian noise, the optimum value of α for a given ϵ is explicit:

$$\begin{aligned} \hat{\alpha}(\epsilon) &= \arg \max_{\alpha \in \mathbb{R}} p(\mathbf{z}|H_1, \alpha, \epsilon) \\ &= \arg \min_{\alpha \in \mathbb{R}} (\mathbf{z} - \alpha \mathbf{s}_\epsilon)' \mathbf{R}^{-1} (\mathbf{z} - \alpha \mathbf{s}_\epsilon) \\ &= \frac{\mathbf{s}_\epsilon^t \mathbf{R}^{-1} \mathbf{z}}{\mathbf{s}_\epsilon^t \mathbf{R}^{-1} \mathbf{s}_\epsilon}; \end{aligned} \quad (5)$$

then the generalized PMF (GPMF) is equal to

$$\hat{\alpha}(\epsilon_0) \mathcal{T}_{\epsilon_0}(\mathbf{z}) = \frac{|\mathbf{s}_{\epsilon_0}^t \mathbf{R}^{-1} \mathbf{z}|^2}{\mathbf{s}_{\epsilon_0}^t \mathbf{R}^{-1} \mathbf{s}_{\epsilon_0}}. \quad (6)$$

B. Subpixel Detectors

Our aim is to build refined detectors that improve the performance of the GPMF by taking into account the variability of the object's signature owing to its random subpixel location. Several solutions may be used. We recall the most popular one first.

1. Generalized-Likelihood-Ratio Test

A ML estimation of the two unknown parameters leads to the generalized-likelihood-ratio test (GLRT):

$$\begin{aligned} \mathcal{L}_g(\mathbf{z}) &= \frac{\max_{(\alpha, \epsilon)} p(\mathbf{z}|H_1, \alpha, \epsilon)}{p(\mathbf{z}|H_0)} \\ &= \frac{p(\mathbf{z}|H_1, \hat{\alpha}_{ML}, \hat{\epsilon}_{ML})}{p(\mathbf{z}|H_0)} \geq \text{threshold}. \end{aligned} \quad (7)$$

It consists in estimating amplitude α and possible object location ϵ by computing

$$\begin{aligned} \hat{\epsilon}_{ML} &= \arg \max_{\epsilon \in \mathcal{E}} p[\mathbf{z}|H_1, \hat{\alpha}(\epsilon), \epsilon] \\ &= \arg \max_{\epsilon \in \mathcal{E}} \frac{|\mathbf{s}_\epsilon^t \mathbf{R}^{-1} \mathbf{z}|^2}{\mathbf{s}_\epsilon^t \mathbf{R}^{-1} \mathbf{s}_\epsilon}. \end{aligned} \quad (8)$$

Then thresholding the estimated filter $\hat{\alpha}_{ML} \mathcal{T}_{\hat{\epsilon}_{ML}}(\mathbf{z})$, where $\hat{\alpha}_{ML} = \hat{\alpha}(\hat{\epsilon}_{ML})$ is given by Eq. (5), yields

$$\hat{\alpha}_{ML} \mathcal{T}_{\hat{\epsilon}_{ML}}(\mathbf{z}) = \frac{|\mathbf{s}_{\hat{\epsilon}_{ML}}^t \mathbf{R}^{-1} \mathbf{z}|^2}{\mathbf{s}_{\hat{\epsilon}_{ML}}^t \mathbf{R}^{-1} \mathbf{s}_{\hat{\epsilon}_{ML}}}. \quad (9)$$

2. Exact-Likelihood-Ratio Test

In a Bayesian approach, we propose to consider the two unknown parameters α and ϵ as manifestations of independent random variables with given

probability-density functions $p(\alpha)$ and $p(\epsilon)$. Then the optimal procedure is the exact-likelihood-ratio test (ELRT).

To compute the density function of data under H_1 and to get the likelihood ratio, we have to integrate the conditional density $p(\mathbf{z}|H_1, \alpha, \epsilon)$ over prior distributions of nuisance random parameters α and ϵ . The likelihood ratio can be expressed as

$$\mathcal{L}(\mathbf{z}) = \frac{p(\mathbf{z}|H_1)}{p(\mathbf{z}|H_0)} = \frac{\int_{\epsilon} \int_{\alpha} p(\mathbf{z}|H_1, \alpha, \epsilon) p(\alpha) p(\epsilon) d\alpha d\epsilon}{p(\mathbf{z}|H_0)}. \quad (10)$$

Given prior distributions $p(\alpha)$ and $p(\epsilon)$, $\mathcal{L}(\mathbf{z})$ is the optimal Neyman–Pearson test whenever α and ϵ really satisfy the models $p(\alpha)$ and $p(\epsilon)$. By default we choose a noninformative prior distribution for α and adopt a uniform distribution inside the pixel for ϵ , which seems to be quite a reasonable assumption for the subpixel target position. So we get

$$\mathcal{L}(\mathbf{z}) \propto \int_{\epsilon} \frac{1}{(\mathbf{s}_\epsilon^t \mathbf{R}^{-1} \mathbf{s}_\epsilon)^{1/2}} \exp\left(\frac{|\mathbf{s}_\epsilon^t \mathbf{R}^{-1} \mathbf{z}|^2}{2 \mathbf{s}_\epsilon^t \mathbf{R}^{-1} \mathbf{s}_\epsilon}\right) d\epsilon. \quad (11)$$

Unfortunately, because of the intricate nonlinear dependence of \mathbf{s}_ϵ on ϵ , explicit integration over ϵ appears not to be tractable, and the probability distribution of $\mathcal{L}(\mathbf{z})$ is not as simple as that of $\mathcal{T}_{\epsilon_0}(\mathbf{z})$. A quadrature approximation is required for computing $\mathcal{L}(\mathbf{z})$, whereas derivation of its density requires Monte Carlo simulations.

3. Approximate Likelihood-Ratio Test

In relation (11), we can approximate the double integral over ϵ to any desired accuracy by using some quadrature rule and evaluating integrand $f(\epsilon|\mathbf{z})$ at discrete samples $\epsilon_k \in \mathcal{E} = [-0.5, 0.5]^2$. But, for the sake of computational efficiency, we propose to use a coarse approximation of likelihood ratio $\mathcal{L}_a(\mathbf{z})$ based on a bidimensional trapezoidal rule that involves only nine positions: the center of the pixel $\epsilon_0 = (0, 0)$; the four half-pixel positions $(0, \pm 0.5)$ and $(\pm 0.5, 0)$, denoted ϵ_k , $k = 1, \dots, 4$; and the four corners $(\pm 0.5, \pm 0.5)$, denoted ϵ_k , $k = 5, \dots, 8$:

$$\mathcal{L}_a(\mathbf{z}) = 1/4 \left[f(\epsilon_0|\mathbf{z}) + 1/2 \sum_{k=1}^4 f(\epsilon_k|\mathbf{z}) + 1/4 \sum_{k=5}^8 f(\epsilon_k|\mathbf{z}) \right]. \quad (12)$$

4. Subspace Model

An alternative to this probabilistic viewpoint can be built on a geometric approach that restricts signal vector $\mathbf{s} = \alpha \mathbf{s}_\epsilon$ to vary in some P -dimensional subspace, with P less than the vector size.¹⁰ The observed data under H_1 are rewritten as

$$\mathbf{z} \simeq \mathbf{S} \mathbf{a} + \mathbf{n} = \sum_{p=1}^P a_p \mathbf{s}_p + \mathbf{n}, \quad (13)$$

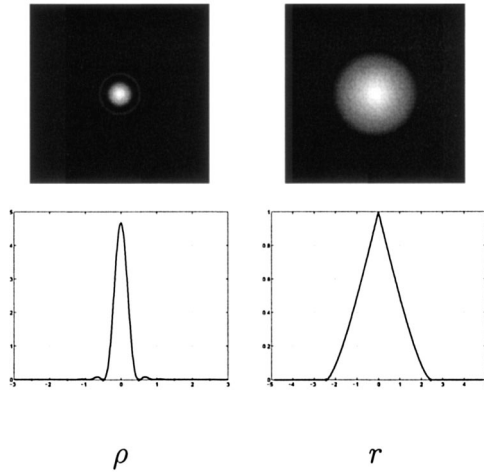


Fig. 4. Left, radial PSF $h_o(u, v)$ (top) and slice along a diameter (bottom). Right, corresponding optical transfer function $\tilde{h}_o(v_u, v_v)$ and slice along a diameter ($r_c = 2.44$).

where structural matrix \mathbf{S} is formed by P independent vectors \mathbf{s}_p . Coefficients a_p of the linear combination are the new parameters that describe the signal's variability. As a result of linearity, the ML estimation of vector \mathbf{a} has an explicit solution (which is identical to the least-squares estimator):

$$\hat{\mathbf{a}}_{\text{ML}} = (\mathbf{S}'\mathbf{R}^{-1}\mathbf{S})^{-1}\mathbf{S}'\mathbf{R}^{-1}\mathbf{z}, \quad (14)$$

and the GLRT amounts to threshold the following statistic:

$$\mathcal{D}(\mathbf{z}) = \mathbf{z}'\mathbf{R}^{-1}\mathbf{S}(\mathbf{S}'\mathbf{R}^{-1}\mathbf{S})^{-1}\mathbf{S}'\mathbf{R}^{-1}\mathbf{z}. \quad (15)$$

Matrix \mathbf{S} depends only on ϵ . α is a scale parameter; in practice, one identifies it by discretizing ϵ , making a singular value decomposition, and retaining singular vectors \mathbf{s}_p that correspond to the P greatest singular values. We chose $P = 1$, which gives better results than higher orders. Therefore, under hypothesis H_1 , $\mathbf{z} \approx a_1\mathbf{s}_1 + \mathbf{n}$, and $\mathcal{D}(\mathbf{z})$ is identical to the GPMF with \mathbf{s}_{ϵ_0} replaced by \mathbf{s}_1 .

3. Application to Optical Imagery

A. Optical System

In our application we can model the imaging system by a diffraction-limited, unaberrated optics with circular aperture and incoherent illumination.^{11,12} Object signal pattern \mathbf{s}_ϵ is then given by the integration of h_o on each pixel [see Eq. (1)], where h_o is the radial point-spread function (PSF) defined by the Airy disk:

$$h_o(u, v) = \frac{1}{\pi} \left[\frac{J_1(\pi\rho r_c)}{\rho} \right]^2, \quad \rho = \sqrt{u^2 + v^2}. \quad (16)$$

J_1 is a Bessel function of the first kind, and $r_c = v_c/v_s$ designates the normalized cutoff frequency (v_s is the sampling frequency and $v_c = D/\lambda$ is the radial cutoff frequency defined by the ratio of the lens's

aperture diameter D to wavelength λ). Figure 4 depicts the two-dimensional PSF and a slice along one diameter as well as their Fourier transform. Common sensor design uses $r_c = 2.44$, so the pixel size is equal to the width of the main lobe of the PSF. However, this implies a downsampling factor $v_n/v_s = 2r_c = 4.88$ (where $v_n = 2v_c$ is the Nyquist frequency). In Subsection 3.B below, we present some numerical results of detection performance that resulted from using this classical sensor design. Examples of image spots \mathbf{s}_ϵ are shown in Fig. 1 for various values of ϵ .

Remark 1. We have the following property:

$$\sum_{(i,j) \in \mathbb{Z}^2} \mathbf{s}_\epsilon[i, j] = \int_{\mathbb{R}^2} h_o(u, v) du dv = 1.$$

B. Numerical Results

The performance of the five classes of detector, the GPMF and the GLRT of α and ϵ , the ELRT, the approximate-likelihood ratio test (ALRT), and finally the GLRT with the subspace model (denoted the SM-GLRT), were compared in terms of ROC curves. We deduced the probabilities of detection and false alarm from the empirical distributions of these statistics under each hypothesis by generating samples of Gaussian noise \mathbf{n} and uniformly distributed ϵ in $\epsilon = [-0.5, 0.5]^2$. The amplitude was assumed to be unknown but set to a constant value α in the simulations because we had no information about a reliable prior distribution $p(\alpha)$.

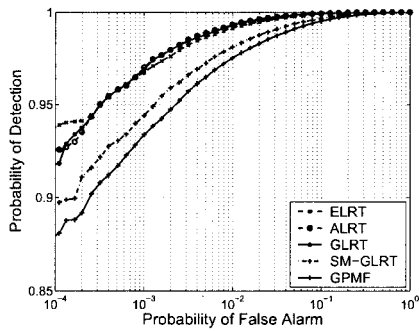
We considered first the Gaussian white noise $\mathbf{n} \sim \mathcal{N}(0, \sigma^2)$. The SNR was then defined by

$$\text{SNR} = 10 \log_{10} \left(\frac{\alpha^2 E}{\sigma^2} \right), \quad E = \int_{\epsilon} \sum_{(i,j) \in \mathbb{Z}^2} (\mathbf{s}_\epsilon[i, j])^2 d\epsilon. \quad (17)$$

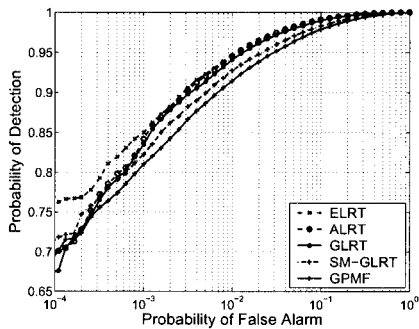
For common sensor design ($r_c = 2.44$), the average energy of the image spot was $E \approx 0.52$. The ROC curves are depicted in Fig. 5 for two SNRs. The figure shows that the GLRT, the ELRT (actually, a refined approximation of it), and the coarse approximation ALRT exhibit significantly better performance than the SM-GLRT and the GPMF. We can also see that the performance gain is greater for high SNR, whereas it tends to be rather small for low SNR and low probability of false alarm. Conversely, if provision of the GPMF, the SM-GLRT, and the ALRT is computationally cheap, provision of the GLRT and the ELRT is much more intensive.

As complementary tests, we tested the five detectors on a fractal background image generated by a variant of the ppmforge software.¹³

The synthesis algorithm depends on autosimilarity parameter H , called the Hurst parameter, which was set to 0.7 in this experiment. The resultant image depicted in Fig. 6 is a realistic simulation of a cloud



$$\text{SNR} = 16.2 \text{ dB } (\alpha/\sigma = 9)$$



$$\text{SNR} = 14.1 \text{ dB } (\alpha/\sigma = 7)$$

Fig. 5. Empirical ROC curves in the Gaussian white-noise case with common sensor design ($r_c = 2.44$) for two different SNRs. These curves were obtained for 9×10^4 instances of noise.

scene. Covariance matrix \mathbf{R} of this stationary background was estimated by empirical correlations of the whole image. We then computed the performance of the various detectors for a given target amplitude as illustrated in Fig. 7. The ROC curves look quite different from those for the white-noise case, but we can see again that the GLRT, the ELRT, and the ALRT exhibit similar performance and provide a significant gain in detection compared with the GPMF and the SM-GLRT.

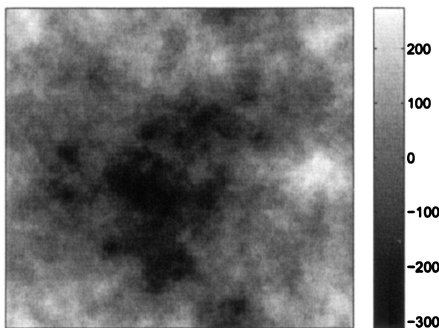


Fig. 6. Simulation of a cloud fractal image of 200×200 pixels (Hurst parameter, $H = 0.7$).

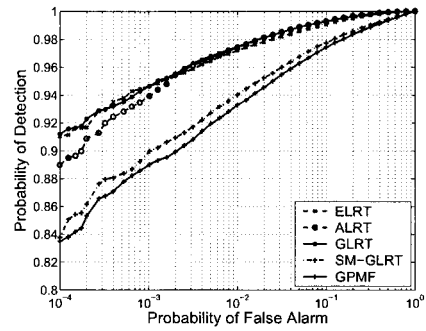


Fig. 7. Empirical ROC curves obtained for the fractal image of Fig. 6 for a true (but assumed unknown) target amplitude $\alpha = 60$ gray levels. The standard deviation of the correlated noise on the whole image is ~ 104 gray levels, and the estimated innovation standard deviation is ~ 4.6 . The following generalized definition of the SNR, $10 \log_{10}(\alpha^2 \int_{\epsilon} \mathbf{s}_{\epsilon}^T \mathbf{R}^{-1} \mathbf{s}_{\epsilon} d\epsilon)$, leads to an estimated SNR value of 18.1 dB.

C. Influence of the Optics

Besides a desire to perfect and evaluate subpixel detectors, one additional motivation for this research was a wish to analyze the influence of aliasing on detection performance. This is why we also tested the detectors on correctly sampled optics to compare their performance with that obtained by use of a common sensor design. In the correctly sampled design, the focal plane is sampled at the Nyquist frequency (implying a denser sensor array or a smaller lens diameter) such that aliasing is suppressed. Parameter r_c of the PSF is equal to 0.5, and the signal energy is now spread over several pixels. By comparison, Fig. 8 presents examples of image spots that correspond to such a design. Detection performance is depicted in Fig. 9 for a SNR of 15 dB. We can see that the choice of detection algorithm is just a moderate factor in this situation. The five detectors exhibit quite similar behavior, but at the same SNR they perform much better than in the aliased case. The gain in P_{fa} amounts at least to a factor of 10 for all the detectors. Such a result speaks in favor of using a denser focal plane for point target detection.

Remark 2. In the presence of aliasing, term $\mathbf{s}_{\epsilon}^T \mathbf{R}^{-1} \mathbf{s}_{\epsilon}$ depend on ϵ , even when the noise is white.

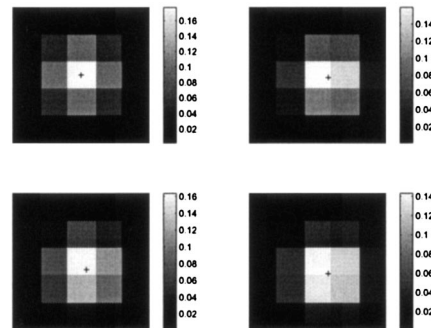
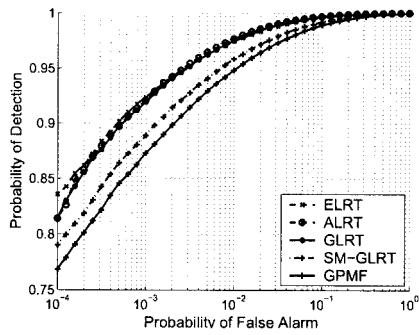
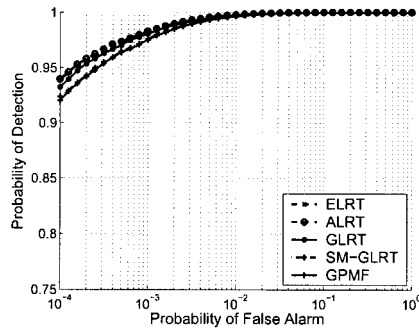


Fig. 8. Examples of image spots corresponding to a correctly sampled optics ($r_c = 0.5$) to be compared with those of Fig. 1.



$$r_c = 2.44$$



$$r_c = 0.5$$

Fig. 9. Empirical ROC curves in the Gaussian white-noise case with common sensor design (top, $r_c = 2.44$) compared with correctly sampled optics (bottom, $r_c = 0.5$) for the same SNR of 15 dB. These curves were obtained for 4×10^5 instances of noise.

For example, in a common sensor design, signal energy $E_\epsilon = \mathbf{s}_\epsilon^t \mathbf{s}_\epsilon$ varies from 0.21 to 0.72. Such is not the case for the correctly sampled optics where E_ϵ is constant and equal to $E \approx 0.08$.

4. Performance of Subpixel Position Estimators

So far we have focused on the detection strategy. In a second step, once a potential target is detected on a given pixel we are interested also in accurate estimation of its subpixel position. Such a problem has already been addressed, in particular for estimation of positions of stars in astronomical applications.¹⁴ Several types of estimator are possible. We consider here the maximum likelihood (ML) estimator and, following the Bayesian approach introduced previously, the posterior mean. It is important to note that signal amplitude α is also unknown and that therefore we have to estimate it or integrate over it. Indeed, it is not valid to suppose that the amplitude is known in the context of the infrared search-and-track algorithm.

The ML estimator of ϵ is given in Eq. (8) by replacement of α with its estimate $\hat{\alpha}$. In fact, $\hat{\epsilon}_{\text{ML}}$ and $\hat{\alpha}_{\text{ML}} = \hat{\alpha}(\hat{\epsilon}_{\text{ML}})$ are identical to joint maximum *a posteriori* (MAP) estimators with noninformative prior distributions on the two parameters.

The PM estimator is defined as

$$\hat{\epsilon}_{\text{PM}} = \int_{\epsilon} \epsilon p(\epsilon | H_1, \mathbf{z}) d\epsilon, \quad (18)$$

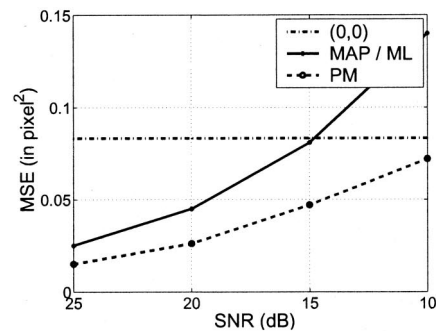
where the posterior law is deduced from Bayes's rule:

$$\begin{aligned} p(\epsilon | H_1, \mathbf{z}) &= \frac{p(\mathbf{z} | H_1, \epsilon) p(\epsilon)}{p(\mathbf{z} | H_1)} \\ &= \frac{p(\epsilon)}{p(\mathbf{z} | H_1)} \int_{\mathbb{R}} p(\mathbf{z} | H_1, \alpha, \epsilon) p(\alpha) d\alpha. \end{aligned} \quad (19)$$

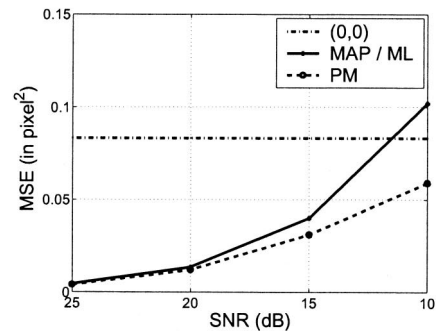
So we have to integrate over α and then over ϵ . As above, we consider a diffuse prior law on \mathbb{R} for α and a uniform law on ϵ for ϵ . We get the following expression in the same way as for the likelihood ratio in relation (11):

$$p(\epsilon | H_1, \mathbf{z}) \propto \frac{1}{(\mathbf{s}_\epsilon^t \mathbf{R}^{-1} \mathbf{s}_\epsilon)^{1/2}} \exp\left(-\frac{|\mathbf{s}_\epsilon^t \mathbf{R}^{-1} \mathbf{z}|^2}{2 \mathbf{s}_\epsilon^t \mathbf{R}^{-1} \mathbf{s}_\epsilon}\right). \quad (20)$$

We studied the performance of these two estimators in terms of average MSE. In practice, optimization or integration over ϵ is approximated numerically for a finite discrete grid of 20×20 values $\epsilon_k \in \epsilon$. Given a true position ϵ^* , we can estimate



$$r_c = 2.44$$



$$r_c = 0.5$$

Fig. 10. Average MSEs of position estimators in the Gaussian white-noise case with common sensor design (top, $r_c = 2.44$) compared with correctly sampled optics (bottom, $r_c = 0.5$). MAP, maximum *a posteriori*.

bias and variance of an estimator $\hat{\epsilon}$ by using Monte Carlo simulations. We consider Gaussian white noise, and we vary the SNR. Figure 10, left, compares ML and PM estimators to the pixel estimator; it is assumed by default that the target location is at the center of the pixel [$\hat{\epsilon} = (0, 0)$], whose MSE is $1/12$. At a favorable SNR the two subpixel estimators are far better than the default estimator, but the gain decreases when noise becomes important. For a SNR of 15 dB, the ML yields an error similar to that of the default estimator, whereas the PM notably has a twice smaller error. By comparison, Fig. 10, right, shows the estimation performances obtained in the unaliased case ($r_c = 0.5$) for equivalent SNRs. ML and PM logically perform better because the signal is correctly sampled.

5. Conclusions and Directions for Future Research

We have presented the problem of detection of subpixel objects embedded in additive Gaussian noise. Subpixel location and signal amplitude were assumed to be unknown. Unknown subpixel location was shown to have a great influence on detection performance in the aliased case, whereas the conventional matched filter neglects it. Thus we derived four types of improved detector, the GLRT, the ELRT, the ALRT, and the SM-GLRT, from the likelihood ratio. We illustrated their performance in comparison with the classic GPMF. Numerical results for both white and correlated noise show that the ELRT, the ALRT, and the GLRT are competitive, whereas the SM-GLRT does not reach the same quality but slightly improves the performance of the GPMF. Use of the ALRT seems to be a good trade-off because it is not so computationally demanding as the ELRT and the GLRT; moreover, the performance gain proves to be only moderate for unaliased optics. This conclusion has important consequences for sensor design. It suggests that the popular design of a pixel that covers the main lobe of the Airy disk exactly is not optimum for point object detection. Future research will consist in studying the robustness of these detectors to real data and ways in which we can take into account non-Gaussian distributions of background noise. As far as the position-estimation problem is concerned, we have demonstrated pro-

spective gains that must also be confirmed with more-realistic data.

References and Notes

1. C. D. Wang, "Adaptive spatial/temporal/spectral filters for background clutter suppression and target detection," *Opt. Eng.* **21**, 1033–1038 (1982).
2. A. Margalit, I. S. Reed, and R. M. Gagliardi, "Adaptive optical target detection using correlated images," *IEEE Trans. Aerosp. Electron. Syst.* **21**, 394–405 (1985).
3. T. Soni, J. R. Zeidler, and W. H. Ku, "Performance evaluation of 2-D adaptive prediction filters for detection of small objects in image data," *IEEE Trans. Image Process.* **2**, 327–340 (1993).
4. X. Yu, L. E. Hoff, I. S. Reed, A. M. Chen, and L. B. Stotts, "Automatic target detection and recognition in multiband imagery: a unified ML detection and estimation approach," *IEEE Trans. Image Process.* **6**, 143–156 (1997).
5. E. A. Ashton, "Detection of subpixel anomalies in multispectral infrared imagery using an adaptive Bayesian classifier," *IEEE Trans. Geosci. Remote Sens.* **36**, 506–517 (1998).
6. I. S. Reed, R. M. Gagliardi, and H. M. Shao, "Application of three-dimensional filtering to moving target detection," *IEEE Trans. Aerosp. Electron. Syst.* **19**, 898–905 (1983).
7. S. D. Blostein and T. S. Huang, "Detecting small, moving objects in image sequences using sequential hypothesis testing," *IEEE Trans. Signal Process.* **39**, 1611–1629 (1991).
8. J. M. Mooney, J. Silverman, and C. E. Caefer, "Point target detection in consecutive frame staring infrared imagery with evolving cloud clutter," *Opt. Eng.* **34**, 2772–2784 (1995).
9. H. L. Van Trees, *Detection, Estimation and Modulation Theory* (Wiley, New York, 1968), Part 1.
10. D. Manolakis and G. Shaw, "Detection algorithms for hyperspectral imaging applications," *Signal Process. Mag.* **19**, 29–43 (2002).
11. J. W. Goodman, *Introduction à l'Optique de Fourier et à l'Holographie* (Masson, Paris, 1972).
12. R. C. Hardie, K. J. Barnard, J. G. Bognar, E. E. Armstrong, and E. A. Watson, "High-resolution image reconstruction from a sequence of rotated and translated frames and its application to an infrared imaging system," *Opt. Eng.* **37**, 247–260 (1998).
13. The ppmforge software is an open-source program originally designed by John Walker and included with the PBMPLUS and NetPBM raster image utilities; ppmforge generates random fractal forgeries of clouds, planets, and starry skies. A manual page can be found at <http://netpbm.sourceforge.net/doc/ppmforge.html>, and the source code is available, for example, at the following web address: http://www.ehynan.com/java_applet/fractal_applet/FractApplet/ppmfcprt/.
14. K. A. Winick, "Cramer–Rao lower bounds on the performance of charge-coupled-device optical position estimators," *J. Opt. Soc. Am. A* **3**, 1809–1815 (1986).